

Hybrid Random FM Waveforms for Enhanced Range Sidelobe Performance

Jonathan Owen¹, David Felton¹, Peter Asuzu², Vincent Amendolare², Shannon Blunt¹

¹ Radar Systems Lab, University of Kansas, Lawrence, KS

² Lincoln Laboratory, Massachusetts Institute of Technology, Lexington, MA

Abstract— Recent work has examined optimization of frequency modulated (FM) waveforms to improve matched filter range sidelobes, while maintaining continuous phase attributes and spectral containment amenable to high power amplification. Through autocorrelation sidelobe minimization of each pulse independently, the range characteristics of a traditional nonlinear FM (NLFM) can be further enhanced. However, the resulting waveforms no longer exhibit the monotonic instantaneous frequency features of NLFM.

Here, random phase perturbations are incorporated into each NLFM prior to optimization – resulting in marginally diverse waveforms. The ensuant waveforms are similar to NLFM (though never explicitly enforced), revealing per-pulse autocorrelation performance resembling that of NLFM. Importantly, because each waveform is distinct from the others, slow time processing results in incoherent range sidelobes as observed for random FM (RFM). This hybrid random FM (HRFM) class demonstrates reduced range sidelobes relative to NLFM. As a consequence of pulse-to-pulse diversity, Doppler sidelobes slightly increase due to range mainlobe modulation (RMM) in trade for the improved range performance.

Keywords—waveform diversity, random frequency modulation (RFM), nonlinear frequency modulation (NLFM).

I. INTRODUCTION

Traditional methods to incorporate range sidelobe minimization into waveform design were explored first in [1], which leveraged the principal of stationary phase to design the instantaneous frequency of chirp waveforms to match power spectrum shapes corresponding to low autocorrelation sidelobes due to their Fourier transform pair. This nonlinear FM (NLFM) design was extended for shaping arbitrary discrete power spectra in [2]. With optimization [3], the spectral match between the NLFM and the desired power spectrum can also be improved. However, a key tenet of NLFM design is a monotonic instantaneous frequency with increasing time – thus mitigating time-frequency interactions to better match the desired power spectrum template. For specific power spectrum shapes, many continuous-time expressions have been derived to describe NLFMs to simplify analysis and/or hardware implementation (see appendix of [4]).

Since then, a plethora of pulsed waveform designs have been examined that minimize matched filter range sidelobes [5], apply a-priori knowledge of the illuminated scene to inform the transmission [6], and diversify waveforms for improved per-pulse and coherent aggregate range estimation [7]. Random FM (RFM) waveforms have noise-like qualities, while maintaining constant amplitude and continuous phase attributes

amenable to high power amplification [7]. Similar to NLFM, RFM design can be improved via optimization of their autocorrelation [5] or power spectrum [8]. Due to pulse-to-pulse varying phase/frequency characteristics, when RFMs are coherently combined they additionally benefit from an incoherent correlation sidelobe averaging that reduces self-interference [7].

A common reference for waveform design is the ambiguity function [11]. The ambiguity function describes the expected range estimate of a moving point scatterer (for a continuum of velocities) after correlating with the transmit waveform matched filter. For analysis of a single pulse, the ambiguity function is often described either as Doppler-tolerant or Doppler-selective (called a “thumbtack” ambiguity). NLFMs exhibit a Doppler tolerant ridge, while RFMs typically exhibit thumbtack behavior [12]. Recalling that ambiguous energy is preserved, individual RFMs cannot attain quite the degree of low sidelobe performance as NLFM near zero Doppler (i.e. autocorrelation). The Doppler-tolerant ridge of the NLFM effectively acts as a “sink” for ambiguous energy, allowing for improved autocorrelation performance.

To maintain Doppler tolerance, waveform designs exist that enforce a similarity constraint to linear FM (LFM) waveforms having a Doppler ridge [13]-[14], with the realized resemblance measurable by a range-Doppler coupling factor [15]. In [5], it was observed that minimization of NLFM autocorrelation sidelobes (without monotonicity constraints) yielded a similar waveform – but now having frequency perturbations that improves sidelobe performance. Of course, reduction of autocorrelation sidelobes inherently pushes energy elsewhere in the ambiguity function, which may not be of concern for sufficiently slow moving scatterers imposing Doppler less than the reciprocal of pulse duration ($f_D \ll 1/T_p$). Likewise, sidelobe minimization may degrade spectral containment [16].

Here, the per-pulse autocorrelation sidelobe optimization outlined in [5] is extended to include a spectral containment constraint. By initialization with NLFMs having small random phase perturbations, each optimized waveform exhibits an improved peak sidelobe level (relative to a standard NLFM) and a marginally nonrepeating phase/frequency structure from pulse-to-pulse. Importantly, the optimization sufficiently diversifies these waveforms to provide incoherent range sidelobes after slow time Doppler processing (akin to RFMs). These hybrid RFM (H-RFM) waveforms demonstrate the per-pulse sidelobes of NLFMs and aggregate performance of RFMs. The lower bound of combined autocorrelation sidelobe

DISTRIBUTION STATEMENT A. Approved for public release. Distribution is unlimited.

This material is based upon work supported by the Dept of the Army under Air Force Contract No. FA8702-15-D-0001. Any opinions, findings, conclusions or recommendations expressed in this material are those of the author(s) and do not necessarily reflect the views of the Dept of the Army.

performance is then described by the optimum spectrally contained power spectrum that minimizes peak sidelobes [10].

II. WAVEFORM OPTIMIZATION

In [16], a discretized constant-modulus waveform model was considered that incorporates a phase modifier quasi-basis function expressed as

$$\mathbf{s} = \frac{e^{j\Phi}}{\sqrt{M}} = \frac{e^{jBx}}{\sqrt{M}} \quad (1)$$

where \mathbf{x} represents $N \times 1$ discrete waveform parameters and \mathbf{B} is the $M \times N$ quasi-basis function, which forms the $M \times 1$ signal phase Φ . The denominator normalizes the signal vector to have unit energy. Here, the quasi-basis is set to an identity matrix $\mathbf{B} = \mathbf{I}$ to form an angle modulated waveform [9], since spectral containment constraints will implicitly limit the intersample phase transitions [8]. The autocorrelation function

$$\mathbf{r} = \mathbf{A}^H (\tilde{\mathbf{A}}\mathbf{s} \odot (\tilde{\mathbf{A}}\mathbf{s})^*) \quad (2)$$

can be represented in terms of the $K \times K$ unitary discrete Fourier transform (DFT) matrix \mathbf{A} and the $K \times M$ truncated (otherwise unitary) DFT matrix $\tilde{\mathbf{A}}$, where $K = 2M - 1$ to represent correlation. Here, we wish to minimize the autocorrelation sidelobes (selected by a binary mask \mathbf{w}_{sl}). The sidelobe performance is sufficiently characterized by the objective function

$$J = \|\mathbf{w}_{sl} \odot \mathbf{r}(\mathbf{x})\|_p^p \quad (3)$$

where $\|\cdot\|_p$ indicates the vector p -norm, $p = 2$ quantifies the integrated sidelobe level (ISL) and $p = 8$ is used to approximately quantify peak sidelobe level (PSL). As noted in [16], waveform spectral containment is necessary. A spectral containment constraint is imposed that controls the power spectrum energy in regions designated by \mathbf{w}_f , which contains ones in selected stopbands and zeros otherwise. The constraint is then expressed as

$$G = \|\mathbf{w}_f \odot (\mathbf{A}\mathbf{s})\|_2^2 - \gamma \|\mathbf{s}\|_2^2 < 0 \quad (4)$$

where γ is the maximum total energy ratio permitted in the designated regions of \mathbf{w}_f , indicating a percent energy occupancy. Here, we select γ to be $\gamma = \mu(\mathbf{1}^T \mathbf{w}_f)/M^2$ where $\mu = 4$ relaxes the constraint. The contained energy low sidelobe (CELSI) optimization is ultimately expressed as

$$\begin{aligned} \min_{\mathbf{x}} & \|\mathbf{w}_{sl} \odot \mathbf{r}(\mathbf{x})\|_p^p \\ \text{s.t. } & \|\mathbf{w}_f \odot (\mathbf{A}\mathbf{s})\|_2^2 - \gamma \|\mathbf{s}\|_2^2 < 0. \end{aligned} \quad (5)$$

The gradient of the objective function is determined as [5]

$$\nabla_{\mathbf{x}} J = 2p \mathbf{B}^T \Im \left\{ \mathbf{s}^* \odot \left[\tilde{\mathbf{A}}^H (\tilde{\mathbf{A}} \mathbf{s} \odot \mathbf{r} \odot \mathbf{w}_{sl})) \right] \right\} \quad (6)$$

and the gradient of the constraint is

$$\nabla_{\mathbf{x}} G = 2 \mathbf{B}^T \Im \{ \mathbf{s}^* \odot (\tilde{\mathbf{A}}^H [(\tilde{\mathbf{A}} \mathbf{s}) \odot \mathbf{w}_f] - \gamma \mathbf{s}) \}. \quad (7)$$

The problem is solved via the augmented Lagrange optimization routine outlined in [17]. The inner gradient descent algorithm applies L-BFGS which is known to converge with minimal

computational cost [18], as implemented in the open source Tensorlab library [19]. To enforce this inequality spectral constraint, the augmented Lagrangian function is posed as

$$\mathcal{L} = J + \left(\lambda + \frac{\mu}{2} G \right) G^+ \quad (8)$$

for λ the Lagrange multiplier and μ a penalty parameter that takes on a large value when the constraint is not satisfied. The function $(\cdot)^+ = \max\{0, \cdot\}$ extracts the positive part of the argument, and results such that iff $G > 0$, the penalty parameter μ increases to subsequently place more emphasis on addressing the constraint violation. The resulting gradient of (8) is

$$\nabla_{\mathbf{x}} \mathcal{L} = \nabla_{\mathbf{x}} J + (\lambda + \mu G)^+ \nabla_{\mathbf{x}} G. \quad (9)$$

Minimization of this Lagrangian gradient descent framework produces waveforms having adequate spectral containment with minimized sidelobes.

III. SIMULATED RESULTS

The selected initialization \mathbf{x}_{init} for the CELSI optimization significantly impacts the resulting waveform. Here, the initial signals are formed by combining an NLFM phase Ψ with random phase perturbations $\Theta \sim U(-\pi, \pi)$ expressed as

$$\mathbf{s}_{init} = e^{j\mathbf{x}_{init}} = e^{j(\Psi + \alpha\Theta)} \quad (10)$$

where $0 < \alpha < 1$ scales Θ to shrink or grow the deviations. For large α , the initialization is sufficiently random such that the optimized waveforms tend toward RFM behavior. For small α , the NLFM phase structure is dominant but the random phase deviations can influence each pulse optimization toward slightly dissimilar local minima to form H-RFM waveforms. These H-RFM waveforms are similar to the initial NLFM waveform (though never explicitly constrained), but the small phase deviations impart sufficient randomness to achieve the benefit of incoherent autocorrelation sidelobe integration upon slow time processing.

The selected NLFM initial waveform that determines Ψ is first defined, which provides a near-optimal deterministic waveform having minimized autocorrelation sidelobes. The CELSI optimized waveform sets, formed by applying (10) to yield both RFM and H-RFM classes, are analyzed in terms of their autocorrelation function, ambiguity function, point-spread function and inter-pulse cross-correlation to demonstrate relevant tradeoffs.

A. Nonlinear FM Waveforms

Spectral shaping of traditional NLFM waveforms is most commonly achieved by applying the principle of stationary phase (POSP) [1]. For an FM waveform of monotonically increasing frequency over time, the instantaneous frequency $f_i(t)$ of the signal can be approximately determined according to the desired spectrum shape $d(f)$, as described in [20]. The choice of spectrum shape impacts the waveform autocorrelation characteristics, surveyed in [21]. For a time-limited waveform, the degree of match to the desired spectrum is never without error. When an NLFM is matched to a spectrum pertaining to low sidelobes, such as a Gaussian, the achieved per-pulse

autocorrelation sidelobe level is approximately $1/(TB)^2$, where TB is the time bandwidth product.

Separately, the limitations of correlation-based processing were assessed by determining the optimum null-constrained power spectrum that minimizes correlation sidelobe levels. Herein, the NLFM is shaped to the discretized optimum spectrum $\hat{\mathbf{d}}_f$ from [10] that minimizes autocorrelation sidelobe levels for a specified mainlobe resolution while maintaining spectral null constraints. This template $\hat{\mathbf{d}}_f$ is found from the convex objective function

$$\begin{aligned} \min_{\mathbf{d}_f} & \| \mathbf{e} - \mathbf{A}^H \mathbf{d}_f \|_{\rho}^{\rho} \\ \text{s. t. } & d_{f,m} \leq \gamma_m \text{ for } m \in \Lambda \\ & 0 \leq d_{f,m} \text{ for } m = 0, 1, \dots, M-1 \end{aligned} \quad (11)$$

where $m = 0, 1, \dots, M-1$ indicates discrete frequency, \mathbf{e} is the desired autocorrelation response (a unit impulse), \mathbf{A} is the $M \times M$ discrete Fourier transform matrix, γ_m is the constrained maximum value for the associated $d_{f,m}$ when m is in the subset Λ (i.e. null constraints), and selection of $\rho = 2$ minimizes ISL whereas $\rho \rightarrow \infty$ minimizes PSL. Different degrees of mainlobe resolution are achievable by replacing \bar{M} rows of \mathbf{A} (corresponding to autocorrelation mainlobe roll-off) with zeros. Here $\gamma_m = 10^{-3}$ (or 30 dB depth), $\rho = 8$ to well-approximate PSL minimization, and $\bar{M} = 5$ are used. The suppressed regions Λ are selected for digital frequencies of $\Lambda \in (-0.5, -0.25) \cup (0.25, 0.5)$. Note that this optimum template that minimizes PSL is closely tied to the Dolph-Chebyshev window [22], though the spectrum obtained in (11) is explicitly spectrally contained and also capable of tuning to minimize ISL (or “in-between” sidelobe metrics for $2 < \rho < \infty$).

Upon calculating the fixed optimal spectrum shape, the NLFM spectrum is matched to $\hat{\mathbf{d}}_f$ by numerically calculating the instantaneous frequency function and thus the deterministic phase function Ψ via the POSP as outlined in [20]. The NLFM waveform represented by $e^{j\Psi}$ exhibits near-optimum sidelobe levels, with residual sidelobe error on the order of $1/(TB)^2$. Because NLFM waveforms are usually repeated, their achieved correlation sidelobe level is static upon slow time combination for Doppler estimation.

B. Comparison of RFM and H-RFM Waveforms

The CELSI optimization routine that solves (5) via (8) and (9) is performed with two initializations described by (10). Here, \mathbf{w}_f selects a stopband in the regions of Λ , while \mathbf{w}_{sl} minimizes sidelobes outside of the selected mainlobe resolution indicated by $\bar{M} = 5$ single-sided roll-off samples. Selecting an initial phase perturbed NLFM with $\alpha = 1$ sufficiently randomizes the phase, so the optimized waveform exhibits noise-like qualities akin to the RFM class. Rather, when $\alpha = 0.5$ the phase deviations introduce variation, but an NLFM structure still remains – thus generating the H-RFM waveform class upon optimization. The optimization is performed for $P = 1000$ waveforms each having $M = 1000$ samples, where each initialization is provided different random perturbations Θ .

The instantaneous frequency structure of 10 optimized RFM ($\alpha = 1$) and H-RFM ($\alpha = 0.5$) are shown in Figure 1, with the frequency structure of the initial NLFM waveform

overlaid for reference. Instantaneous frequency indicates time-frequency characteristics and the maximum phase transition between waveform samples. As noted in [8], the optimized angle modulated waveforms both implicitly demonstrate a maximum phase transition between $-\pi/2$ and $\pi/2$ (with only occasional excursions) due to power spectrum containment, allowing for near-continuous phase required for high power amplification. The mean power spectra for $P = 1000$ pulses of NLFM, RFM, and H-RFM waveforms are shown in Figure 2, with the power spectrum $\hat{\mathbf{d}}_f$ determined from (11) overlaid.

Interestingly, the CELSI optimization is never explicitly informed of the spectrum $\hat{\mathbf{d}}_f$ – rather the PSL metric is directly minimized for individual waveforms. Because the H-RFM maintains structure from the initial NLFM waveform (matched to $\hat{\mathbf{d}}_f$), the resulting local optima are influenced to the NLFM spectrum shape as indicated in Figure 2. In contrast, the RFM are sufficiently randomized to realize major deviations from the NLFM shape, as indicated by increased spectral flattening.

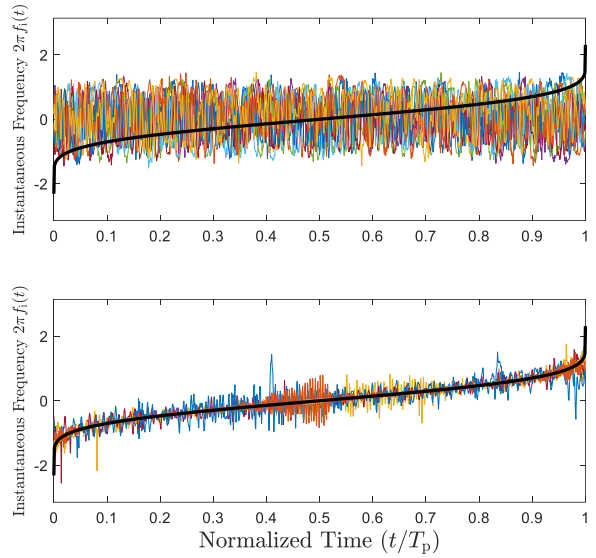


Figure 1: Instantaneous Frequency of 10 RFM waveforms (multicolored, top) and 10 H-RFM waveforms (multicolored, bottom) and an NLFM waveform (black).

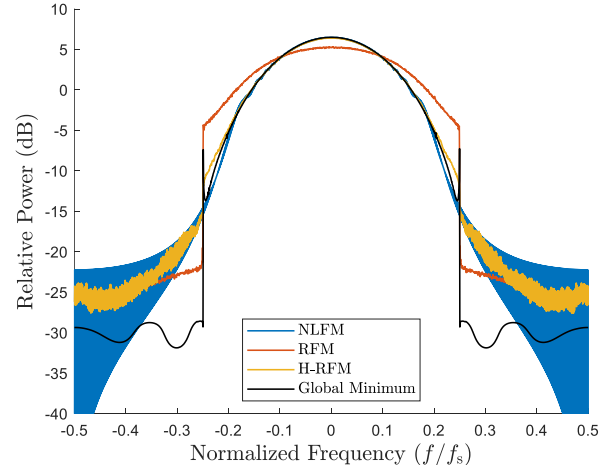


Figure 2: Mean power spectrum $\frac{1}{P} \sum_{v,p} |\tilde{A}s_p|^2$ of NLFM, RFM, H-RFM, and optimum $\hat{\mathbf{d}}_f$ for $M = 1000$ samples and $P = 1000$ pulses.

It is well known that a deterministic signal autocorrelation $\mathbf{r} = \mathbf{s} * \mathbf{s}$ and power spectrum $\mathbf{r}_f = |\tilde{\mathbf{A}}\mathbf{s}|^2$ are Fourier transform pairs, such that $\mathbf{r} = \mathbf{A}^H|\tilde{\mathbf{A}}\mathbf{s}|^2$. Due to linearity of the Fourier transform operator, a pair likewise exists between the mean autocorrelation and the mean power spectrum across P pulses:

$$\frac{1}{P} \sum_{\forall p} \mathbf{r}_p = \mathbf{A}^H \left(\frac{1}{P} \sum_{\forall p} |\tilde{\mathbf{A}}\mathbf{s}_p|^2 \right). \quad (12)$$

Waveforms having spectral shapes that adhere closest to $\hat{\mathbf{d}}_f$ in the mean power spectrum implicitly exhibit minimized autocorrelation sidelobes after coherent integration. The RMS autocorrelation indicates typical per-pulse sidelobe performance, expressed as $\sqrt{\frac{1}{P} \sum_{\forall p} |\mathbf{r}_p|^2}$.

The RMS autocorrelation of each waveform class are illustrated in Figure 3. The RMS PSL of the RFM is -37.55 dB, while the NLFM exhibits -46.78 dB and the H-RFM achieves -50.00 dB. In agreement with [5] the H-RFM improves on the PSL relative to the NLFM by 3.22 dB. Additionally, the H-RFM achieves an RMS PSL improvement of 12.45 dB relative to the RFM waveforms. The notable difference in RMS PSL performance between the RFM and H-RFM is simply understood by examining their respective mean ambiguity functions shown in Figure 4, determined via

$$\chi(t, f_D) = \sum_{\forall p} \left| \int s_p^*(\tau) s_p(t - \tau) e^{j2\pi f_D t} d\tau \right|^2. \quad (13)$$

Noting that the total ambiguous energy is conserved [11], the H-RFM can minimize zero-Doppler range/delay sidelobes by driving energy into other Doppler regions. The RFM waveforms alternatively maintains uniform range-Doppler sidelobes across the entire space. The H-RFM Doppler tolerance is similar to that of NLFM waveforms [12].

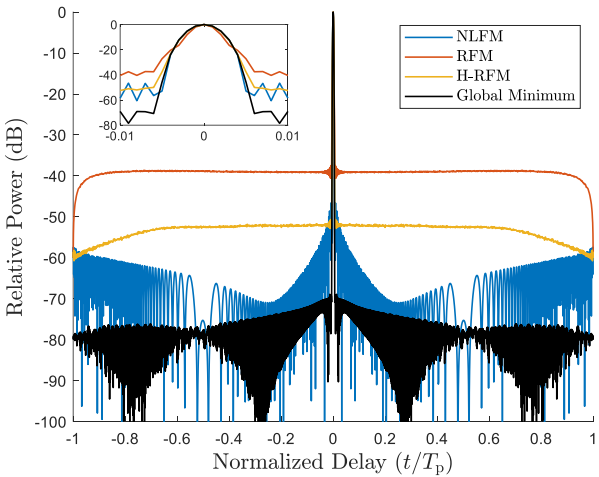


Figure 3: Root-mean-squared autocorrelation $\sqrt{\frac{1}{P} \sum_{\forall p} |\mathbf{r}_p|^2}$ of NLFM, RFM, H-RFM and optimum $\mathbf{A}^H \hat{\mathbf{d}}_f$ for $M = 1000$ samples and $P = 1000$ pulses, indicating per-pulse range sidelobe performance.

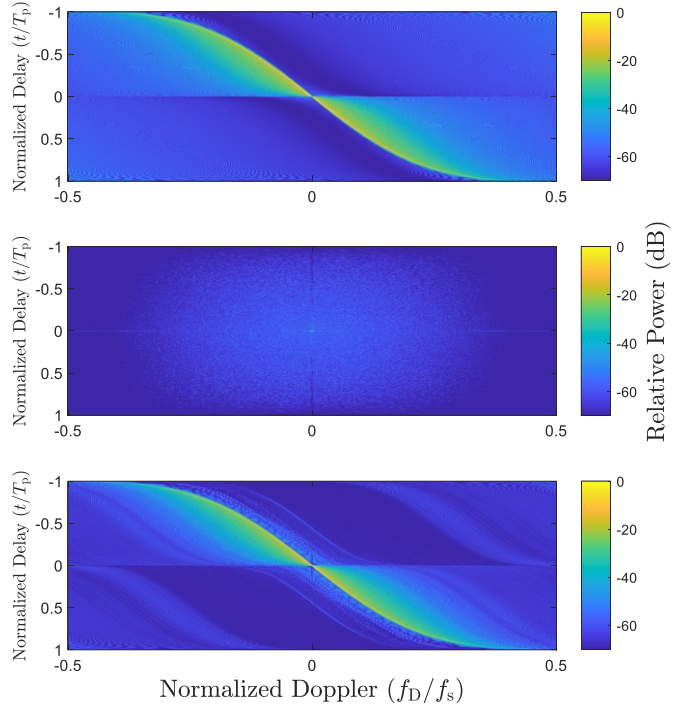


Figure 4: Mean ambiguity function of NLFM (top), RFM (middle), and H-RFM (bottom) for $M = 1000$ samples/pulse and $P = 1000$ pulses. The RFM is Doppler selective, while the NLFM and H-RFM are Doppler tolerant.

The non-repeating and optimized nature of H-RFM provides another beneficial quality. Because each H-RFM waveform has a slightly dissimilar power spectrum, the mean power spectrum can more closely match to an optimal solution. Alternatively, NLFM demonstrate Fresnel ripple in their power spectrum which hinders the degree of spectral match. By the Fourier relation in (12), waveform sets which exhibit a smooth mean power spectrum similar to $\hat{\mathbf{d}}_f$ will achieve minimal mean autocorrelation sidelobe levels. The mean autocorrelation of NLFM, RFM, and H-RFM are shown in Figure 5. The mean PSL of the RFM is -39.40 dB, while the NLFM still exhibits -46.78 dB and the H-RFM achieves -58.33 dB. The H-RFM improves on the PSL relative to the NLFM by 11.55 dB. Additionally, the H-RFM achieves a mean PSL improvement of 18.93 dB relative to the RFM waveforms.

The combined range sidelobe performance improvement of H-RFM in comparison to NLFM is a direct consequence of the increased degrees of freedom introduced by marginal pulse diversity, which effectively counteracts Fresnel ripple in the mean power spectrum. To produce H-RFM waveforms, other optimization algorithms may be applicable [8]. Similarity constraints could feasibly control the degree of achieved phase randomness in the H-RFM waveform structure [13],[14]. Of important note, the phase deviations introduced via (10) alone (without optimization) do not improve the mean power spectrum and autocorrelation, since the aggregate response trends to the initial NLFM waveform as $\mathbb{E}\{e^{j(\Psi+\alpha\theta)}\} \approx e^{j\Psi}$. The waveform optimization realizes the smooth mean power spectrum that provides enhanced autocorrelation features.

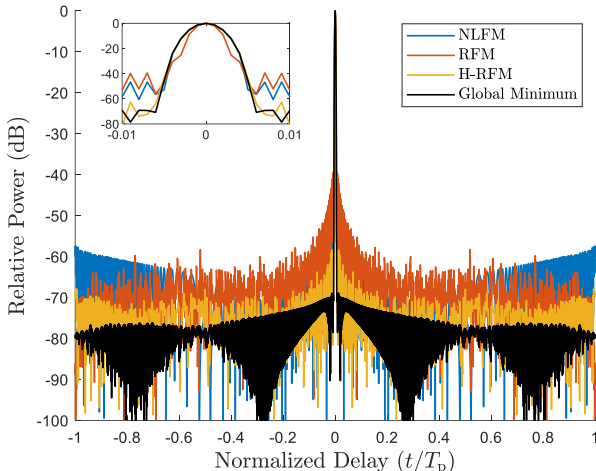


Figure 5: Mean autocorrelation $\frac{1}{P} \sum_{p=1}^P \mathbf{r}_p$ of NLFM, RFM, H-RFM, and optimum $\mathbf{A}^H \hat{\mathbf{d}}_f$ for $M = 1000$ samples and $P = 1000$ pulses, indicating coherently combined range sidelobe performance.

A known difference between near-deterministic and noise-like waveforms lies in their cross-correlation performance. NLFM waveforms are often pulsed in a repeated manner, indicated ambiguities in range and Doppler dependent on the selected pulse repetition frequency (PRF). RFM waveforms have demonstrated low cross-correlation between adjacent pulses that provides opportunity for range disambiguation [24]. H-RFM waveforms are observed to exhibit slight decorrelation between pulses. The cross-correlation between pulse p and the subsequent pulse $p + 1$ are shown in Figure 6, for both RMS (indicating per-pulse performance) and mean (indicating aggregate performance) metrics. As anticipated, the NLFM is entirely correlated pulse-to-pulse. The RFM exhibits an RMS cross-correlation peak of -25.81 dB and mean peak of -46.38 dB indicating separability. In contrast, the H-RFM demonstrates a cross-correlation RMS peak of -1.93 dB and mean peak of -2.20 dB indicating degraded separability.

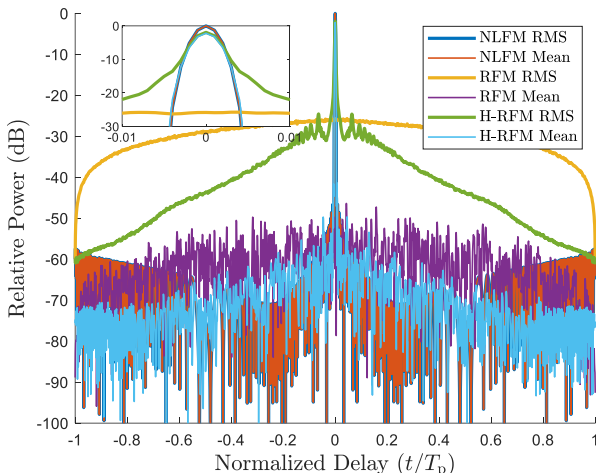


Figure 6: Root-mean-squared and mean cross-correlation of NLFM, RFM, and H-RFM waveforms between pulse p and $p + 1$ for $P = 1000$ pulses.

Because RFM waveforms introduce range sidelobe modulation (RSM), it is useful to examine the point spread functions (PSF) of each waveform set, which is defined as

$$\Upsilon(t, f_D) = \left| \sum_{p=1}^P w_p \left(\int s_p^*(\tau) s_p(t - \tau) d\tau \right) e^{-j2\pi(\frac{f_D}{f_{\text{PRF}}})p} \right|^2 \quad (14)$$

where w_p represents a slow time taper weight for the p^{th} pulse. Here, a Taylor window is applied to mitigate Doppler sidelobes. The PSF of the NLFM waveform set demonstrates typical range-Doppler sidelobes and a sparse background in Figure 7. The PSF of the RFM and H-RFM waveform sets are shown in Figures 8 and 9, respectively. The RFM waveforms produced via the CELSI optimization demonstrate anticipated RSM [7]. Both RFM and H-RFM exhibit range mainlobe modulation (RMM) due to variations in the pulse-to-pulse mainlobe rolloff resulting from the CELSI algorithm. RMM induces a band of energy across Doppler upon slow time-Doppler processing [4]. For the CELSI optimization, the RFM exhibits a peak RMM of -34.00 dB, while the H-RFM has a peak RMM of -51.08 dB (4.3 dB less than the NLFM autocorrelation PSL). This RMM can be alleviated by using template based waveform optimizations that implicitly minimize mainlobe dissimilarity [8], joint range-Doppler sidelobe minimization [25], or least squares mismatched filter pulse compression in exchange for slight mismatch loss [10].

IV. CONCLUSIONS

Through constrained minimization of peak sidelobe levels, H-RFM waveforms having characteristics of both NLFM and RFM classes were generated and characterized. The tradeoffs between RFM and H-RFM have been explored in terms of autocorrelation performance, cross-correlation waveform separability, and Doppler tolerance/selectivity. With sufficient degrees-of-freedom, H-RFM can achieve a mean power spectrum and autocorrelation approaching the optimum bound from [10] with fewer pulses than are required for RFM.

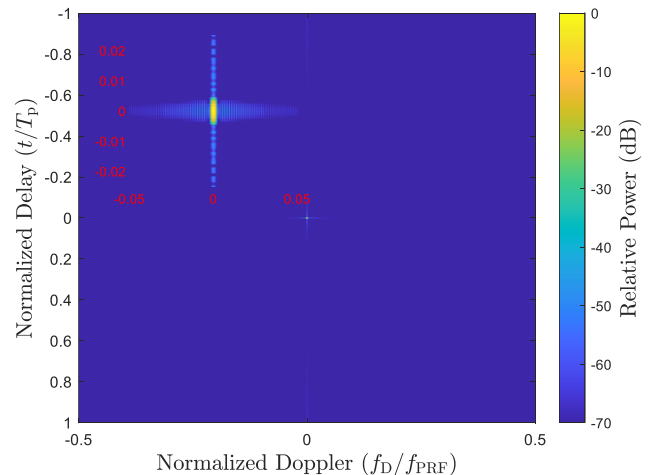


Figure 7: Point-spread function of $P = 1000$ repeated NLFM pulses with slow time Taylor window.

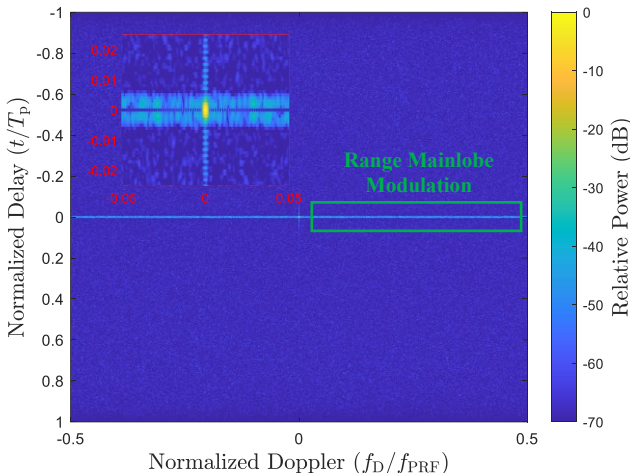


Figure 8: Point-spread function of $P = 1000$ diverse RFM pulses with slow time Taylor window.

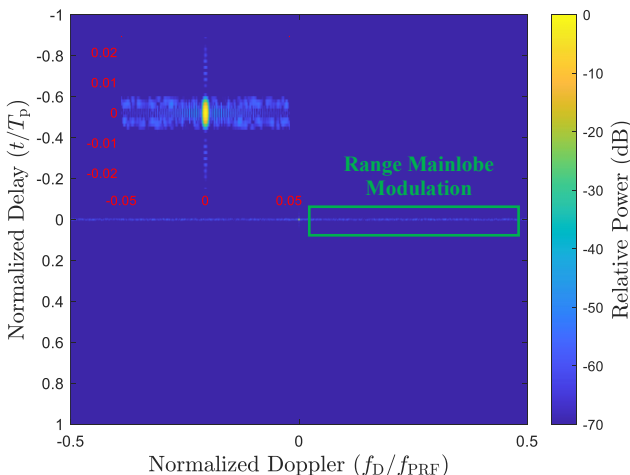


Figure 9: Point-spread function of $P = 1000$ diverse H-RFM pulses with slow time Taylor window.

REFERENCES

- [1] J. Klauder, A. Price, S. Darlington, W. Albersheim, "The theory and design of chirp radars," *The Bell System Technical Journal*, vol. 39, no. 4, pp. 745-808, July 1960.
- [2] E. Fowle, "The Design of FM Pulse Compression Signals," *IEEE Trans. of Information Theory*. 1964.
- [3] A. Doerry, "Generating nonlinear FM chirp waveforms for radar". Sandia Report. September 2006.
- [4] J. Owen, "Real-Time Cognitive Sense-and-Notch Radar," Ph.D. Dissertation, University of Kansas, May 2023.
- [5] C. A. Mohr, P. M. McCormick, C. A. Topliff, S. D. Blunt and J. M. Baden, "Gradient-Based Optimization of PCFM Radar Waveforms," *IEEE Trans. on Aerospace and Electronic Systems*, vol. 57, no. 2, pp. 935-956, April 2021.
- [6] D. Herr, P. Raju, J. Stiles, "Information theoretic waveform design with applications to adaptive-on-transmit radar," *IET Radar, Sonar & Navigation*, 20 October 2023.
- [7] S. Blunt et al., "Principles and Applications of Random FM Radar Waveform Design," *IEEE Aerospace and Electronic Systems Mag.*, vol. 35, no. 10, pp. 20-28, 1 Oct. 2020.
- [8] J. Owen, C. Jones, P. McCormick, D. Felton, M. Heintzelman, J. Quirk, S. Blunt, "Analysis of Spectrally Efficient Random FM Radar Waveforms", 2024 IEEE Int'l Radar Conf., Rennes, France, 2024.
- [9] J. Roberts, "Angle modulation: the theory of system assessment," *IEEE Telecommunications Series*. Jan. 1977.
- [10] J. W. Owen, P. M. McCormick, C. C. Jones, S. D. Blunt, "On the Optimality of Spectrally Notched Radar Waveform & Filter Designs," 2023 IEEE Radar Conf., San Antonio, TX.
- [11] Nadav Levanon, Eli Mozeson, "Radar Signals", IEEE, 2004.
- [12] J. Quirk, R. Chang, J. Owen, S. Blunt, P. McCormick, "A Simple yet Effective Metric for Assessing Doppler Tolerance," in *IEEE Trans. on Radar Systems*. 2023.
- [13] A. De Maio, S. De Nicola, Y. Huang, Z. -Q. Luo and S. Zhang, "Design of Phase Codes for Radar Performance Optimization With a Similarity Constraint," in *IEEE Trans. on Signal Processing*, vol. 57, no. 2, pp. 610-621, Feb. 2009.
- [14] A. De Maio, Y. Huang and M. Piezzo, "A Doppler Robust Max-Min Approach to Radar Code Design," *IEEE Trans. on Signal Processing*, vol. 58, no. 9, pp. 4943-4947, Sept. 2010.
- [15] L. Cohen, Time-Frequency Analysis. Electrical engineering signal processing. Prentice Hall PTR, 1995.
- [16] B. White, M. Heintzelman, S. Blunt, "Alternative "Bases" for gradient-based optimization of parameterized FM radar waveforms," 2023 IEEE Radar Conf., San Antonio, TX.
- [17] J. Nocedal, S. Wright, *Numerical Optimization*. Springer Science & Business Media, 2006.
- [18] D.C. Liu, J. Nocedal, "On the limited memory BFGS method for large scale optimization," *Mathematical Programming*, vol. 45, pp. 503–528, Aug. 1989.
- [19] N. Vervliet, O. Debals, L. Sorber, M. Van Barel, L. De Lathauwer, Tensorlab 3.0, <https://www.tensorlab.net/>, Mar. 2016.
- [20] E. Fowle, "The design of FM pulse compression signals," *IEEE Trans. on Information Theory*, vol. 10, no. 1, pp. 61–67, Jan. 1964.
- [21] G. Jin et al., "An Advanced Nonlinear Frequency Modulation Waveform for Radar Imaging With Low Sidelobe," in *IEEE Trans. on Geoscience and Remote Sensing*, vol. 57, no. 8, pp. 6155-6168, Aug. 2019.
- [22] Y. Zhang, W. Wang, R. Wang, Y. Deng, G. Jin and Y. Long, "A Novel NLFM Waveform With Low Sidelobes Based on Modified Chebyshev Window," *IEEE Geoscience and Remote Sensing Letters*, vol. 17, no. 5, pp. 814-818, May 2020.
- [23] G. Jin, Y. Deng, Y. Long, W. Wang, Y. Zhang and R. Wang, "The Design of Orthogonal Waveform Suiting for Synthetic Aperture Radar Imaging," 2019 6th Asia-Pacific Conf. on Synthetic Aperture Radar, Xiamen, China, 2019.
- [24] J. Jakabosky, S.D. Blunt, B. Himed, "Spectral-shape optimized FM noise radar for pulse agility," *IEEE Radar Conf.*, Philadelphia, PA, May 2016.
- [25] D. Felton, J. Owen, S. Blunt, "Random FM waveforms jointly optimized for delay-Doppler ambiguity shaping," 2025 IEEE Int'l Radar Conf., Atlanta, GA.